EPTT 2024
Escola de Primavera de Transição e Turbulência

ABCM
Associação Brasileira de Engenharia e Ciências Mecânicas

EPTT-2024-0030
Development and validation of a linear stability analysis tool for compressible shear flows

Carlos A. Rodrigues
William R. Wolf
School of Mechanical Engineering, University of Campinas, Campinas, SP 13083-860, Brazil
wolf@fem.unicamp.br

Abstract. *We develop a computational tool to study modal and non-modal linear stability analysis of compressible flows at a range of Mach numbers. For this, the generalized eigenvalue problem is solved by constructing the discrete operator for the linearized Navier-Stokes equations employing fourth-order finite difference schemes. In a first stage, the linear stability solutions are validated by comparing spectra for well-known cases, such as the Poiseuille flow. This is followed by a non-modal study performed via the resolvent analysis. The comparison of the compressible operator at low Mach number for the Poiseuille flow shows great correspondence in both modal and non-modal analysis. The non-normality of the problem investigated is seen in the resolvent analysis and by analyzing only the resonant limit. A validation of the operator is also presented for a compressible boundary layer at Mach numbers 1 and 6. Results are compared in terms of spectra and neutral curves, the latter confirms the presence of the second instability mode arising in compressible flows at high Mach numbers.*

Keywords: *Linear stability analysis, compressible flows, modal analysis, non-modal analysis*

1. INTRODUCTION

Linear stability analysis plays a key role in the understanding, control and optimization of aerodynamic flows. In aeronautical applications, small disturbances in the flow can lead to transition from laminar to turbulent due to the inherent high Reynolds numbers. Moreover, compressibility effects may also impact the stability properties of the fluidic systems. Studies of fluid stability date back to the 19th century by Rayleigh, who made advances in the study of inviscid flows. Lees (1947) extended Rayleigh's theorems to include compressibility effects and, later, Mack (1984) carried out numerical analyses of instabilities for compressible flows. This latter author noticed the existence of higher instability modes when the phase velocity was supersonic, currently called Mack modes.

One possible way to study instabilities in aerodynamic flows consists in performing high-fidelity numerical simulations, which are able to resolve the temporal and spatial evolution of disturbances in the flow. This approach usually involves high computational costs and requires accurate numerical methods to solve the Navier-Stokes equations (Lomax *et al.*, 2001). Another approach employed for studies of flow stability consist in employing linear stability theory (LST) with normal modes (Juniper *et al.*, 2014) or global analysis for 2D and 3D flows (Theofilis, 2011). Some of these global studies have been applied to airfoils (Wang *et al.*, 2019). This methodology is based on assumptions such as small disturbances (linearity) and infinite-time (asymptotic) considerations. Although 2D and 3D flows can be analyzed under the perspective of LST through biglobal and triglobal approaches, much can be gained in the understanding of the flow system by local (1D) analyses, which are computationally inexpensive. Such approaches permit investigations of the temporal or spatial evolution of small disturbances superposed in an equilibrium point of the system (base flow).

Studies of non-modal stability analysis have been gaining prominence in recent years. Unlike the classical modal LST, which focuses only on the eigenvalue spectra and respective modes, the non-modal methodology allows a broader overview of complex interactions that occur in shear flows, for example, effects of transient growth and pseudo-resonances (Schmid and Brandt, 2014). This approach allows the understanding of transition effects that occur in linearly stable systems (in the context of Lyapunov) and may also be employed for flow control strategies under the resolvent analysis perspective.

In this work, we develop a linear stability tool that permits modal and non-modal analyses of compressible flows at a range of Mach numbers. For this, we solve the equations described in (Mack, 1984) and (Hanifi *et al.*, 1996), building a discrete operator for the linearized Navier-Stokes equations. As a first step, we validate the linear stability solutions com-

paring spectra for well-known flow setups such as the Poiseuille (Schmid and Brandt, 2014) and compressible boundary layer flows (Özgen and Kırcalı, 2008). Then, a non-modal study is performed via the resolvent analysis. Finally, local analyses are presented for high Mach number viscous flows over a flat plate showing the complex wave velocity on a stability curve map, displaying the presence of the Mack mode for a high Mach number case.

2. Governing compressible equations

The Navier-Stokes equations for a viscous, heat conducting, perfect gas are presented below. The symbol $*$ denotes dimensional quantities and the overbar denotes instantaneous quantities. Equations (1)-(4) represent the continuity, momentum, and energy equations, followed by an equation of state for ideal gases, and the strain-rate and viscous stress tensor terms, respectively

$$\frac{\partial \overline{\rho}^*}{\partial t^*} + \frac{\partial}{\partial x_j^*}(\overline{\rho}^* \overline{u}_j^*) = 0, \tag{1}$$

$$\frac{\partial \overline{u}_i^*}{\partial t^*} + \overline{u}_j^* \frac{\partial \overline{u}_i^*}{\partial x_j^*} = \frac{1}{\overline{\rho}} \frac{\partial \overline{\tau}_{ij}^*}{\partial x_j^*}, \tag{2}$$

$$\overline{\rho}^* c_v^* \left(\frac{\partial \overline{T}^*}{\partial t^*} + \overline{u}_j^* \frac{\partial \overline{T}^*}{\partial x_j^*} \right) = \frac{\partial}{\partial x_j^*} \left(\overline{\kappa}^* \frac{\partial \overline{T}^*}{\partial x_j^*} \right) + \overline{\tau}_{ij}^* \overline{e}_{ij}^*, \tag{3}$$

$$\overline{P}^* = \overline{\rho}^* R^* \overline{T}^*, \tag{4}$$

$$\overline{e}_{ij}^* = \frac{1}{2} \left(\frac{\partial \overline{u}_i^*}{\partial x_j^*} + \frac{\partial \overline{u}_j^*}{\partial x_i^*} \right), \tag{5}$$

and

$$\overline{\tau}_{ij}^* = 2\overline{\mu}^* \overline{e}_{ij}^* + \left[\frac{2}{3} (\overline{\lambda}^* - \overline{\mu}^*) \overline{e}_{kk}^* - \overline{P}^* \right] \delta_{ij}. \tag{6}$$

Here, $u_i = (u_1, u_2, u_3) = (u, v, w)$ represents the velocity vector, and $x_i = (x_1, x_2, x_3) = (x, y, z)$ provides the spatial coordinates in the streamwise, wall-normal and spanwise directions, respectively. The temperature, pressure, and density are represented by T, P, and ρ, respectively. The coefficient of thermal conductivity is given by κ, the gas constant is R, the specific heat at constant volume is c_v (assumed constant), the second coefficient of viscosity is λ (given by 1.5 times the bulk viscosity coefficient), and the dynamic viscosity is μ. The time is given by t, and δ_{ij} is the Kronecker delta. The superscript $*$ indicates dimensional quantities.

To linearize the set of equations above, the instantaneous flow quantities are decomposed into mean plus perturbation terms as in Eq.(7), and the last three terms are functions only of temperature, so they can be written as in Eq. (8).

$$(\overline{u_i}, \overline{\rho}, \overline{T}, \overline{P}, \overline{\mu}, \overline{\kappa}, \overline{\lambda}) = (U_i, \rho, T, P, \mu, \kappa, \lambda) + (u_i, \rho^{'}, \theta, p, \mu^{'}, \kappa^{'}, \lambda^{'}), \tag{7}$$

$$(\mu^{'}, \kappa^{'}, \lambda^{'}) = \left(\frac{d\mu}{dT}, \frac{d\kappa}{dT}, \frac{d\lambda}{dT} \right) \times \theta. \tag{8}$$

The fluctuation quantities are functions of time and spatial coordinates, while the mean ones are function of the spatial coordinates only. In this work, a parallel flow assumption is considered. Moreover, the present flows homogeneous along spanwise direction. Hence, the mean flow quantities are functions of the wall-normal coordinate only. Then, the flow governing equations are written in nondimensional form using the following relations: $u_i = u_i^*/U_e$, $\rho = \rho^*/\rho_e$, $T = T^*/T_e$, $\mu = \mu^*/\mu_e$, $\lambda = \lambda^*/\lambda_e$, $\kappa = \kappa^*/\kappa_e$, $p = p^*/(R^* \rho_e T_e)$, $x_i = x_i^*/l$; where the subscript "e" refers to the freestream (edge of the boundary layer) quantities and l is a reference length scale. These terms are replaced in Eqs. (1) to (3) with the mean-flow terms being subtracted. The dimensionless parameters appearing in the equations are the Reynolds number $Re = \rho_e l U_e / \mu_e$, the ratio of specific heats $\gamma = c_p^*/c_v^*$, the local Mach number at the edge of boundary layer $M = U_e / \sqrt{\gamma R^* T_e}$ and the Prandtl number $Pr = c_p^* \mu_e / \kappa_e$. More details about the present formulation can be found in (Mack, 1984).

2.1 Normal-mode equations

This section presents the linearized equations for a compressible viscous flow. Equations (1) to (3) are solved for a flow with homogeneous conditions in the streamwise and spanwise directions. As a consequence, this allows the application of Fourier modes in these directions

$$\{q\} = (u, v, w, \rho^{'}, \theta)^T = (\hat{u}, \hat{v}, \hat{w}, \hat{\rho}^{'}, \hat{\theta})^T exp(i\alpha x + i\beta z). \tag{9}$$

This step introduces streamwise and spanwise wavenumbers α and β which simplify the linearized equations. These, in turn, can be rewritten using the state vector $\{q\}$ and the operators $[R]$ and $[L]$ as Eq. (10)

$$[R]\frac{\partial}{\partial t}\{\hat{q}\} = [L]\{\hat{q}\}. \tag{10}$$

After introducing Eq. (9), the linearized equations can be written for the density, u, v, and w velocity components, and temperature, as:

$$\frac{\partial}{\partial t}\hat{\rho} = -\left[i\alpha\rho\hat{u} + (D\rho + \rho D)\hat{v} + i\beta\rho\hat{w} + i(\alpha U + \beta W)\hat{\rho}\right], \tag{11}$$

$$\begin{aligned}\frac{\partial}{\partial t}\hat{u} = &\left\{ - i\alpha U - i\beta W + \frac{1}{\rho Re}\left[\mu\left(- 2\alpha^2 + D^2 - \beta^2\right) - \frac{2}{3}(\lambda-\mu)\alpha^2 + \frac{d\mu}{dT}DTD\right]\right\}\hat{u}\\
&+\left\{ - DU + \frac{1}{\rho Re}\left[i\alpha\mu D + \frac{2}{3}(\lambda-\mu)i\alpha D + \frac{d\mu}{dT}DTi\alpha\right]\right\}\hat{v} + \left\{\frac{1}{\rho Re}\left[- \mu\alpha\beta - \frac{2}{3}(\lambda-\mu)\alpha\beta\right]\right\}\hat{w}\\
&+\left\{\frac{-i\alpha T}{\rho\gamma M^2}\right\}\hat{\rho} + \left\{\frac{-i\alpha}{\gamma M^2} + \frac{1}{\rho Re}\left[\frac{d\mu}{dT}\left(DUD + D^2U\right) + \frac{d^2\mu}{dT^2}DTDU\right]\right\}\hat{\theta},\end{aligned} \tag{12}$$

$$\begin{aligned}\frac{\partial}{\partial t}\hat{v} = &\left\{\frac{1}{\rho Re}\left[i\alpha\mu D + \frac{2}{3}(\lambda-\mu)i\alpha D + \frac{2}{3}\left(\frac{d\lambda}{dT} - \frac{d\mu}{dT}\right)DTi\alpha\right]\right\}\hat{u}\\
&+\left\{ - i\alpha U - i\beta W + \frac{1}{\rho Re}\left[\mu\left(2D^2 - \alpha^2 - \beta^2\right) + \frac{d\mu}{dT}2DTD + \frac{2}{3}(\lambda-\mu)D^2\right.\right.\\
&\left.\left.+\frac{2}{3}\left(\frac{d\lambda}{dT} - \frac{d\mu}{dT}\right)DTD\right]\right\}\hat{v} + \left\{\frac{1}{\rho Re}\left[\mu i\beta D + \frac{2}{3}(\lambda-\mu)i\beta D + \frac{2}{3}\left(\frac{d\lambda}{dT} - \frac{d\mu}{dT}\right)DTi\beta\right]\right\}\hat{w}\\
&+\left\{\frac{-(DT + TD)}{\rho\gamma M^2}\right\}\hat{\rho} + \left\{\frac{-(D\rho + \rho D)}{\rho\gamma M^2} + \frac{1}{\rho Re}\left[\frac{d\mu}{dT}i(\alpha DU + \beta DW)\right]\right\}\hat{\theta},\end{aligned} \tag{13}$$

$$\begin{aligned}\frac{\partial}{\partial t}\hat{w} = &\left\{\frac{1}{\rho Re}\left[- \mu\alpha\beta - \frac{2}{3}(\lambda-\mu)\alpha\beta\right]\right\}\hat{u}\\
&+\left\{ - DW + \frac{1}{\rho Re}\left[i\beta\mu D + \frac{2}{3}(\lambda-\mu)i\beta D + \frac{d\mu}{dT}DTi\beta\right]\right\}\hat{v}\\
&+\left\{ - i\alpha U - i\beta W + \frac{1}{\rho Re}\left[\mu\left(- \alpha^2 + D^2 - 2\beta^2\right) - \frac{2}{3}(\lambda-\mu)\beta^2 + \frac{d\mu}{dT}DTD\right]\right\}\hat{w}\\
&+\left\{\frac{-i\beta T}{\rho\gamma M^2}\right\}\hat{\rho} + \left\{\frac{-i\beta}{\gamma M^2} + \frac{1}{\rho Re}\left[\frac{d\mu}{dT}\left(DWD + D^2W\right) + \frac{d^2\mu}{dT^2}DTDW\right]\right\}\hat{\theta},\end{aligned} \tag{14}$$

and

$$\begin{aligned}\frac{\partial}{\partial t}\hat{\theta} = &\left\{\frac{M^2\gamma(\gamma-1)}{\rho Re}2\mu DUD - (\gamma-1)i\alpha T\right\}\hat{u}\\
&+\left\{ - DT + \frac{M^2\gamma(\gamma-1)}{\rho Re}\left[2\mu DU(i\alpha) + 2\mu DW(i\beta)\right] - (\gamma-1)TD\right\}\hat{v}\\
&+\left\{\frac{M^2\gamma(\gamma-1)}{\rho Re}2\mu DWD - (\gamma-1)i\beta T\right\}\hat{w} + \left\{0\right\}\hat{\rho} + \left\{ - i\alpha U - i\beta W\right.\\
&\left.+\frac{\gamma}{\rho RePr}\left[\kappa\left(D^2 - \alpha^2 - \beta^2\right) + \frac{d^2\kappa}{dT^2}(DT)^2 + \frac{d\kappa}{dT}\left(2DTD + D^2T\right)\right]\right.\\
&\left.+\frac{M^2\gamma(\gamma-1)}{\rho Re}\frac{d\mu}{dT}\left[(DU)^2 + (DW)^2\right]\right\}\hat{\theta}.\end{aligned} \tag{15}$$

In the equations above, the term $D = \frac{d}{dy}$ and it represents derivatives with respect to the non-homogeneous wall-normal flow direction in the present studies.

2.2 Stability analysis via the eigenspectrum

For the study of the flow stability, we apply a Laplace transform to Eq. (10) assuming the exponential time dependence as

$$\hat{q} = \tilde{q} e^{-i\Omega t}. \tag{16}$$

This transformation leads to an eigenvalue problem, where $\omega = -i\Omega$:

$$\omega[R]\{\tilde{q}\} = [L]\{\tilde{q}\}. \tag{17}$$

The analysis of the eigenvalues of this linear system will give us information about the modal (Lyapunov) stability. Hence, it will be possible to verify if the dynamical system at hand is stable or unstable in the infinite time sense. However, this methodology cannot account for the interaction among the modes that could lead to transition in a finite time. Such investigation can be performed by the use of non-modal analysis.

2.3 Transient growth and resolvent norms

Shear flows have linear operators which depict non-normality of eigenvectors. This signifies that non-modal effects can be relevant in a finite time sense due to interaction of such modes and transient growth of disturbances, even in linearly stable flow systems. This effect could trigger transition to turbulence and, hence, it is important to investigate the conditions that result in maximum energy amplification of disturbances. As shown by (Schmid and Brandt, 2014), a measure of transient growth can be computed as

$$G(t) = ||exp(tL)||_E^2 = ||exp(L_E)||_2^2, \tag{18}$$

where

$$[L_E] = \big([H][E][V]\big)[\Lambda]\big([H][E][V]\big)^{-1}. \tag{19}$$

Here, through application of a Chu norm Hanifi *et al.* (1996), the matriz $[E]$ is written as

$$[E] = diag\left(\rho, \rho, \rho, \frac{T}{\rho\gamma M^2}, \frac{\rho}{\gamma(\gamma-1)TM^2}\right). \tag{20}$$

The matrix Λ is diagonal, and contains the eigenvalues of $[L]$, and **V** is the matrix of eigenvectors. The matrix $[H]$ accounts for the integration weights due to grid stretching. In summary, the transient growth is measured using an energy norm that can be subsequently rewritten in terms of an Euclidean norm (denoted here by the subscript 2). Finally, the latter can be computed using a singular value decomposition (SVD).

The resolvent formalism is obtained by considering a forcing term **f** into Eq. (10) and introducing a supplementary equation **g**. The former represents a system forcing, i.e., an external perturbation in the system, while the latter permits the observation of some particular quantity, such as the kinetic energy of the system. The matrices **B** and **C** determine the input and output quantities, for example, how the system responds in a particular variable with respect to forcing applied to another one. For this approach, the dynamics are governed by the following linear system

$$\frac{d}{dt}\{q\} = [L]\{q\} + [B]\{f\}, \tag{21}$$

$$g = [C]\{q\}. \tag{22}$$

Assuming the forcing term as a harmonic driver $f = \hat{f}\, exp(i\Omega t)$, and due to the linearity of the governing equations, the output can also be represented by $g = \hat{g}\, exp(i\Omega t)$. With this, the resolvent norm is given by.

$$R(\omega) = \max_{\hat{f}} \frac{||\hat{g}||_E^2}{||\hat{f}||_E^2} = |||[C](i\omega[I] - [L])^{-1}[B]||_E^2 = |||[C](i\omega[I] - [L_E])^{-1}[B]||_2^2 \tag{23}$$

3. Results

This section presents results computed for canonical test cases. Results are obtained using a fourth-order explicit centered discretization of the wall-normal spatial derivatives (Lomax *et al.*, 2001). For boundary layers, where the flow is unconfined towards the freestream, the grid generation employs a fixed stretching ratio ζ for $i = 0 : N-1$ as in Eq. (24). In the present approach, the number of points N is not controlled, but a function of the domain size "l", the stretching ratio, and the distance of the first point to the wall "Δy_0" as in Eq. (25).

$$y_{i+1} = yi + \Delta y \zeta^i\,, \tag{24}$$

$$N = \frac{\log\left\{\left(\frac{l-\Delta y_0}{\Delta y_0}\right)(\zeta - 1) + 1\right\}}{\log\{\zeta\}} + 1\,. \tag{25}$$

3.1 Poiseuille flow

Poiseuille flow data from Schmid and Brandt (2014) is first used to validate the linear analysis for a low Mach number flow. For this flow, the boundary conditions at both walls ($y = -1$ and $y = 1$) are set as $\hat{u} = \hat{v} = \hat{w} = \hat{\theta} = 0$. So the eigenvalue problem is solved and the spectrum can be compared for a low Mach number ($M = 0.1$) and Prandtl $Pr = 0.71$. The base flow is given by the parabolic streamwise velocity profile $U(y) = 1 - y^2$. In the present compressible formulation, the mean spanwise velocity and temperature profiles are null and constant (equal to one), respectively.

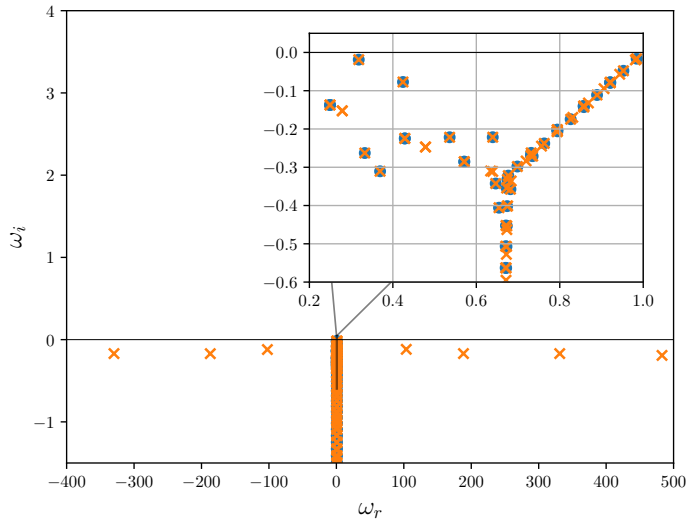

Figure 1. Comparison of eigenvalues for Poiseuille flow. Results from (Schmid and Brandt, 2014) (blue) and the present work (orange) using the parameters $Re = 2000$, $\alpha = 1$ and $\beta = 0.25$. For the present compressible flow, $M = 0.1$.

In Fig. 1, it is possible to observe that the compressible flow solution has more eigenvalues and two more branches to the left and right. This observation is due to the higher number of points used for the fourth-order accuracy discretization when compared with spectral Chebyshev polynomials used by Schmid and Brandt (2014), and also because the energy equation creates "N" additional eigenvalues that are not present in the incompressible solution from the reference. All the eigenvalues are confined in the stable half-plane and a good agreement is seen between the incompressible and compressible solutions.

The non-modal stability is also studied to verify the amplification levels given by the resolvent analysis. The resolvent norm is calculated in Fig. 2 for both cases and it is also evaluated for the resonant limit, given by the inverse of the minimal distance of the forcing frequency $||1/(\omega - \lambda)||$. As one can see, results are also in good agreement for this study. While the resonant limit results show amplification solely due to the most unstable frequencies, the resolvent norm shows that non-normality is present for a range of frequencies. In this case, strong amplification of disturbances is observed between the two most unstable poles of the system.

3.2 Compressible boundary layer

A compressible boundary layer flow is also investigated. The first step of the investigation consisted in testing similarity solution equations for the compressible boundary layers. The formulations from (Toro *et al.*, 1997), (Oz and Kara, 2021) and (Özgen and Kırcalı, 2008) were tested and only the latter showed inflection points for the second derivative of velocity near the plate. These inflection points play an important role in the stability phenomena. In order to capture the near-wall gradients of the velocity profile, mesh stretching is applied to the present stability analysis.

As shown in Fig. (3), the mesh has to be sufficiently refined to resolve the inflection point near the wall. In order to determinate the adequate mesh parameters, an analysis of grid convergence is performed in terms of the eigenspectra. Results are shown in Fig. (4) and, if the stretching factor or the wall-resolution are too high, unstable non-physical eigenvalues appear in the horizontal branches of the spectrum. For these eigenvalues to stay stable, the semi-infinite domain requires an additional boundary condition compared to the Pouisuelle case, i.e., the density perturbation $\rho^{'}(y \rightarrow \infty) = 0$. A Newman boundary condition on the farfield was also tested and the results did not change, what agrees with analysis from by Hamada *et al.* (2023). Overall, Fig. (4) shows that the discrete part of the spectrum converge for the tested meshes, with one unstable mode.

After the mesh convergence study, the base flow is defined and the program is tested for the flow investigated by Freitas (2019). The simulation parameters are $M = 1$, $Re = 3000$, $Pr = 0.7$ and $\alpha = 0.04413$. The mesh for this problem has $l = 300$, $\Delta y_0 = 0.1\%$ of U_{99}, $\zeta = 0.6\%$ of U_{99}. The result for the unstable eigenvalue is $\omega = 0.0124752 + 0.0008894j$

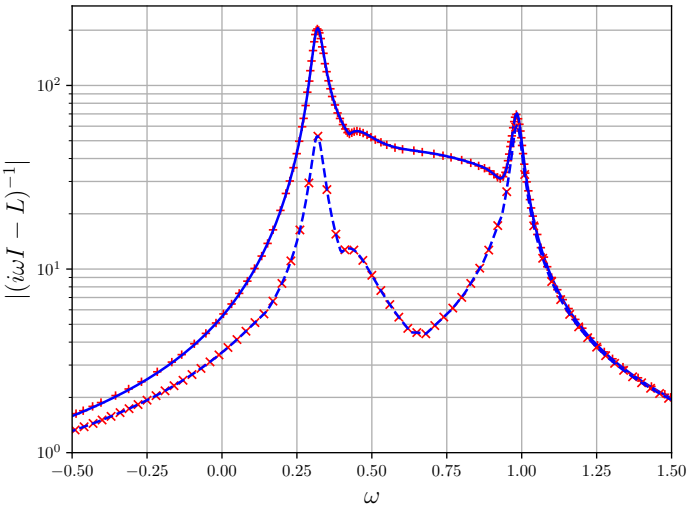

Figure 2. Comparison of resolvent norm for Poiseuille flow for parameters $Re = 2000$, $\alpha = 1$ and $\beta = 0.25$. The blue lines are the solution for the incompressible flow from Schmid and Brandt (2014) and the red symbols are computed by the present compressible flow operator at $M = 0.1$. The dashed line and corresponding symbols represent the resonant limit for both cases.

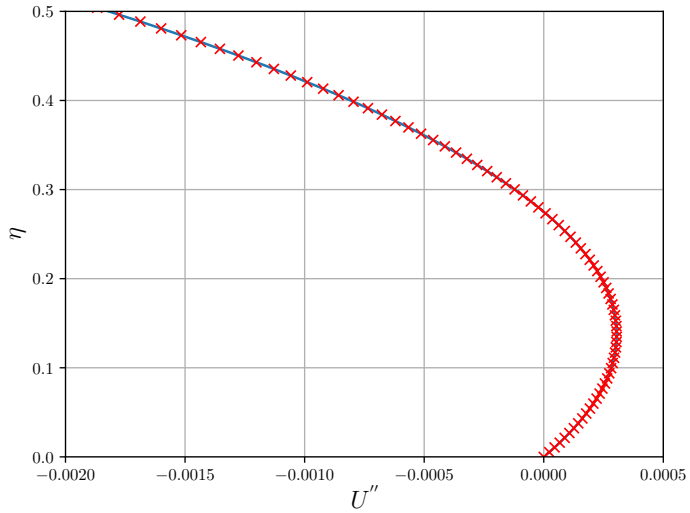

Figure 3. Second derivative of the velocity profile for $M = 1$. The blue line is the similarity solution and the red symbols show the the mesh resolution with appropriate stretching.

using approximately one thousand points, which gives a precision of 10^{-5} compared to the result of Freitas (2019), obtained with 16000 points. Another case computed with the same parameters, but $\alpha = 0.0433$ is also compared with Freitas (2019) (private communication) and the results are shown in the eigenspectrum of Fig. (5). In this plot, results show an excellent agreement for the discrete eigenvalues and for the continuous spectrum. Differences are only noticed on the lateral branches, but one should remind of the different techniques employed in the solution. Results are also compared for a range of streamwise wavenumbers α as shown in Fig. (6), where $c_i = \omega_i/\alpha$ is the complex wave velocity that gives the growth rate.

Comparing only the unstable eigenvalue, the relative error is around 0.21%. The other stable eigenvalues also show good correspondence in Fig. (5). The two horizontal continuous eigenvalues are the ones that differ, but (Hanifi *et al.*, 1996) showed that they do not contribute for transient growth energy, being sensitive to the mesh parameters.

Finally, the complex wave velocity is calculated for a higher Mach number and the stability neutral curves for two-dimensional perturbations are analyzed. The $M = 6$ flow is chosen because it depicts a second mode of instability and, when comparing Fig. (7) with the plot from (Özgen and Kırcalı, 2008) it shows great correspondence of results. For example, two critical values of Reynolds number, $Re_{cr1} \approx 185$ and $Re_{cr2} \approx 830$ are found and these values agree with those calculated by (Özgen and Kırcalı, 2008).

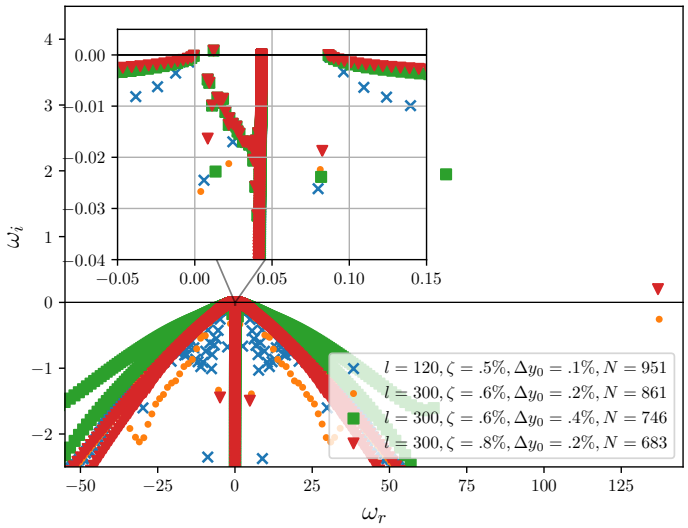

Figure 4. Mesh convergence analysis for $M = 1$.

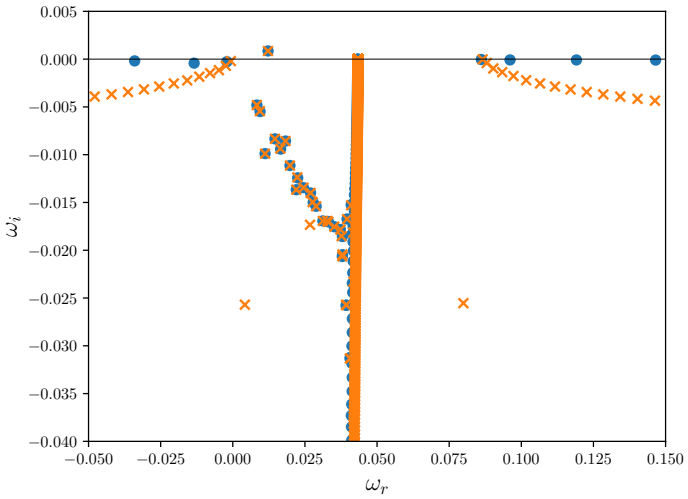

Figure 5. Comparison of eigenvalues for compressible boundary layer flow for parameters $Re = 3000$, $M = 1$, $\alpha = 0.0433$ and $\beta = 0$. The blue symbols are the solution from Freitas (2019) while the orange symbols are the present results.

4. Conclusions

We develop and validate a tool for local linear stability analysis of compressible flows. Results of the Poiseuille flow show a good comparison against the literature for an incompressible case, both in terms of normal and non-normal analyses. The compressible solution has more eigenvalues than the incompressible one due to the presence of the energy equation.For the compressible boundary layer solution, the analysis shows that the results are very sensitive to the base flow and the mesh discretization. For example, mesh refinement can generate unstable eigenvalues on the horizontal branches that would leave to a non-physical Lyapunov instability. The mesh for the compressible semi-infinite domain requires restricting density perturbations in the farfield. Moreover, the stability curve shows the presence of a second unstable mode.

5. ACKNOWLEDGEMENTS

The authors would like to thank Dr. R. B. Freitas for the data provided to compare the results and for the feedback. The authors also thank G. Y. Hamada for the helpful discussions.

6. REFERENCES

Freitas, R.B., 2019. *"Estudo de diferentes ferramentas para análise de estabilidade linear modal em escoamentos incompressíveis e compressíveis"*. Ph.D. thesis, Universidade Federal Fluminense.

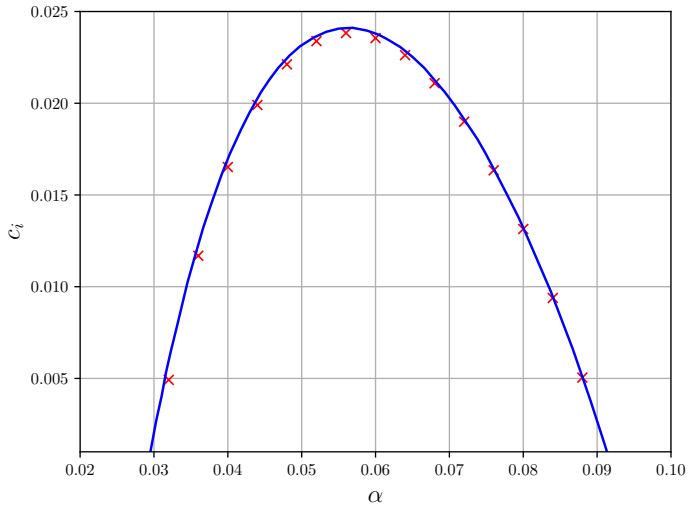

Figure 6. Comparison of complex wave velocity for $Re = 3000$, $M = 1$ and $\beta = 0$. The blue line is the current solution while the red symbols are extracted from Freitas (2019) .

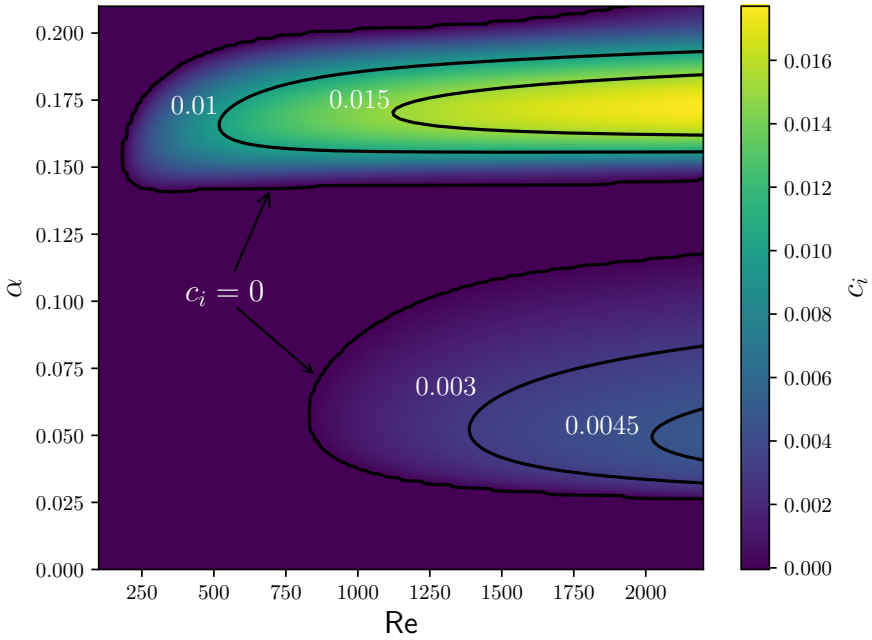

Figure 7. Stability curves for two-dimensional disturbances $M = 6$.

Hamada, G.Y., Wolf, W.R., Pitz, D.B. and Alves, L.S.d.B., 2023. "Stability and receptivity analyses of mixed convection in unstably stratified horizontal boundary layers". *Journal of Fluid Mechanics*, Vol. 961, p. A10.

Hanifi, A., Schmid, P.J. and Henningson, D.S., 1996. "Transient growth in compressible boundary layer flow". *Physics of Fluids*, Vol. 8, No. 3, pp. 826–837.

Juniper, M.P., Hanifi, A. and Theofilis, V., 2014. "Modal stability theory: lecture notes from the flow-nordita summer school on advanced instability methods for complex flows, stockholm, sweden, 2013". *Applied Mechanics Reviews*, Vol. 66, No. 2, p. 024804.

Lees, L., 1947. "The stability of the laminar boundary layer in a compressible fluid". Technical Report NACA-TR-876, Nasa.

Lomax, H., Pulliam, T.H., Zingg, D.W., Pulliam, T.H. and Zingg, D.W., 2001. *Fundamentals of computational fluid dynamics*, Vol. 246. Springer.

Mack, L.M., 1984. "Boundary-layer linear stability theory". *Agard rep*, Vol. 709, No. 3, pp. 1–3.

Oz, F. and Kara, K., 2021. "A cfd tutorial in julia: Introduction to compressible laminar boundary-layer flows". *Fluids*, Vol. 6, No. 11, p. 400.

Özgen, S. and Kırcalı, S.A., 2008. "Linear stability analysis in compressible, flat-plate boundary-layers". *Theoretical and*

Computational Fluid Dynamics, Vol. 22, pp. 1–20.

Schmid, P.J. and Brandt, L., 2014. "Analysis of fluid systems: Stability, receptivity, sensitivitylecture notes from the flow-nordita Summer school on advanced instability methods for complex flows, Stockholm, Sweden, 2013". *Applied Mechanics Reviews*, Vol. 66, No. 2.

Theofilis, V., 2011. "Global linear instability". *Annual Review of Fluid Mechanics*, Vol. 43, pp. 319–352.

Toro, P., Rusak, Z., Nagamatsu, H., Myrabo, L., Toro, P., Rusak, Z., Nagamatsu, H. and Myrabo, L., 1997. "Self-similar compressible laminar boundary layers". In *35th Aerospace Sciences Meeting and Exhibit*. p. 767.

Wang, J., Ziade, P., Huang, G. and Sullivan, P.E., 2019. "Bi-global stability analysis on a NACA 0025 airfoil at a Reynolds number of 100,000". In *Eleventh International Symposium on Turbulence and Shear Flow Phenomena (TSFP11)*. Begel House Inc.

7. RESPONSIBILITY NOTICE

The authors are the only responsible for the printed material included in this paper.